nature nanotechnology

LETTERS

https://doi.org/10.1038/s41565-018-0092-4

Calcium-dependent molecular fMRI using a magnetic nanosensor

Satoshi Okada[1,5], Benjamin B. Bartelle[1,5], Nan Li[1], Vincent Breton-Provencher[2,3], Jiyoung J. Lee[1], Elisenda Rodriguez[1], James Melican[1], Mriganka Sur[2,3] and Alan Jasanoff[1,2,4]*

Calcium ions are ubiquitous signalling molecules in all multicellular organisms, where they mediate diverse aspects of intracellular and extracellular communication over widely varying temporal and spatial scales[1]. Though techniques to map calcium-related activity at a high resolution by optical means are well established, there is currently no reliable method to measure calcium dynamics over large volumes in intact tissue[2]. Here, we address this need by introducing a family of magnetic calcium-responsive nanoparticles (MaCaReNas) that can be detected by magnetic resonance imaging (MRI). MaCaReNas respond within seconds to [Ca^{2+}] changes in the 0.1–1.0 mM range, suitable for monitoring extracellular calcium signalling processes in the brain. We show that the probes permit the repeated detection of brain activation in response to diverse stimuli in vivo. MaCaReNas thus provide a tool for calcium-activity mapping in deep tissue and offer a precedent for the development of further nanoparticle-based sensors for dynamic molecular imaging with MRI.

In the brain, variations in extracellular calcium ion concentrations ($[Ca^{2+}]_o$) are associated with synaptic activity, in which the voltage-triggered influx of extracellular Ca^{2+} is involved in electrical and chemical signalling[3,4]. The consequent reduction of $[Ca^{2+}]_o$ from resting levels near 1 mM, in turn, tends to depress synaptic activity via the extracellular calcium-sensing receptor[5,6] or through direct interactions with glutamate and γ-aminobutyric acid receptor subtypes[7]. Regional extracellular calcium levels are anticorrelated with population-wide intracellular calcium concentrations ($[Ca^{2+}]_i$), though $[Ca^{2+}]_o$ exhibits slower and more diffuse dynamics than $[Ca^{2+}]_i$ (refs [3,8,9]). Behaviourally relevant extracellular calcium changes can last for tens of seconds, with activity-dependent fluctuations that push $[Ca^{2+}]_o$ to concentrations as low as 100 μM (ref. [6]); even slower variations of $[Ca^{2+}]_o$ correlate to sleep–wake transitions[10]. Abnormal Ca^{2+} signalling has been implicated in numerous brain disorders, such as epilepsy and Alzheimer's disease[11], but despite its significance in normal and pathological brain function, basic questions about the phenomenology and mechanisms associated with extracellular Ca^{2+} remain.

An imaging probe to measure extracellular calcium in vivo could be of great value in both basic scientific and medical contexts. Of particular interest is the possibility of using such a probe to map brain activity; this could constitute a molecularly specific analogue to functional MRI (fMRI), a widely used brain-imaging approach that usually detects neurophysiology indirectly via changes in blood flow[2]. Fluorescent Ca^{2+} sensors can be used to measure $[Ca^{2+}]_o$ levels, but most existing compounds have binding constants that are too high for optimal sensing in the 0.1–1.0 mM range; like other optical probes, they are also unsuitable for typical applications in deep tissue. MRI-detectable calcium probes, which include calcium-responsive nanoparticle sensors tuned to other $[Ca^{2+}]$ ranges, have been developed for non-invasive applications[12–14], but none has yet been shown to reveal calcium dynamics in vivo. One of the challenges in constructing a calcium sensor suitable for monitoring $[Ca^{2+}]_o$ is the need for a sensor mechanism that transduces relatively modest analyte fluctuations into discernible changes in the image signal. Such sensitivity is particularly hard to achieve using small-molecule sensors, which usually exhibit binding isotherms that span two orders of magnitude in $[Ca^{2+}]$ (ref. [15]). For this reason, we sought to improve on previous approaches by exploiting the highly cooperative sensing mechanism afforded by reversible magnetic nanoparticle clustering, which can produce large changes in T_2-weighted MRI signals over relatively narrow ionic concentration ranges[2].

To achieve an appropriate sensitivity, a new MaCaReNa probe was engineered using synaptotagmin proteins, which are components of the synaptic neurotransmitter-release machinery that naturally respond to 0.1–1.0 mM changes in $[Ca^{2+}]$ (ref. [1]) and that have not previously been applied for MRI calcium sensing. Each synaptotagmin monomer contains two ~15 kDa calcium-binding C2 domains. Calcium binding to these domains promotes further complex formation with the anionic lipid phosphatidylserine (PS), a component of the plasma-membrane inner leaflet. This interaction can drive the clustering of PS-containing lipid vesicles at Ca^{2+} concentrations above ~0.2 mM (ref. [16]), suitable for monitoring $[Ca^{2+}]_o$.

MaCaReNa sensors based on this effect were prepared by mixing the fused C2 domains of synaptotagmin 1 (C2AB) with lipid-coated iron oxide nanoparticles (LCIOs) (Fig. 1a). The C2AB moieties were expressed and purified from bacteria[17] and the nanoparticles were prepared by coating oleate-stabilized magnetic iron oxide cores with a 7:3 mixture of phosphatidylcholine (PC) and PS (see Methods). Initial tests were performed with combinations that contained 1 nM nanoparticles (100 μM Fe) and 2.5 μM C2AB. Ca^{2+}-dependent aggregation of the sensor components was measured by dynamic light scattering (DLS) in artificial cerebrospinal fluid (aCSF) with or without 1 mM Ca^{2+}. The observed hydrodynamic diameters were 35 ± 1 and 262 ± 14 nm, respectively, in low versus high calcium conditions. Mg^{2+} concentration changes produced no discernible effects in DLS, which demonstrates the specificity of Ca^{2+} dependence (Supplementary Fig. 1). Atomic force microscopy

[1]Department of Biological Engineering, Massachusetts Institute of Technology, Cambridge, MA, USA. [2]Department of Brain & Cognitive Sciences, Massachusetts Institute of Technology, Cambridge, MA, USA. [3]Picower Institute for Learning and Memory, Massachusetts Institute of Technology, Cambridge, MA, USA. [4]Department of Nuclear Science & Engineering, Massachusetts Institute of Technology, Cambridge, MA, USA. [5]These authors contributed equally: S. Okada, B. B. Bartelle. *e-mail: jasanoff@mit.edu

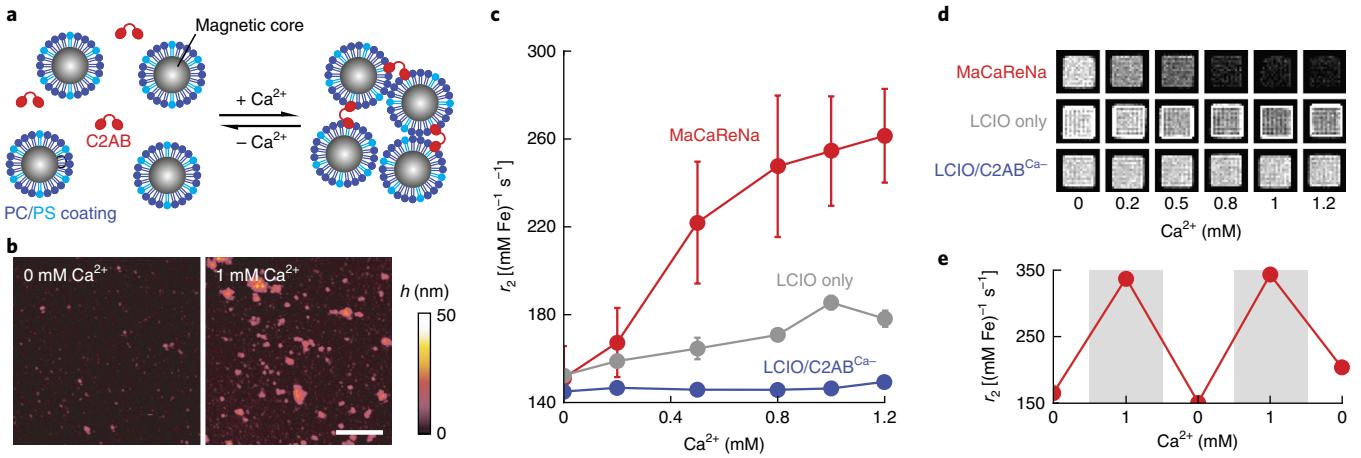

Fig. 1 | Design and in vitro characterization of MaCaReNas. a, Schematic of the sensor design based on LCIOs and C2AB. **b**, AFM of MaCaReNas imaged after exposure to 0 or 1 mM Ca^{2+}. Scale bar denotes 500 nm and colour scale denotes sample height (*h*). **c**, The red titration curve shows r_2 values as a function of [Ca^{2+}] in aCSF, which indicates MaCaReNa responsiveness to calcium concentrations characteristic of the brain extracellular space (mean ± s.e.m., $n = 3$). LCIOs alone (grey) or in the presence of $C2AB^{Ca-}$ (blue) display little responsiveness to Ca^{2+}. **d**, T_2-weighted images ($TR/TE = 2000/72$ ms) of MaCaReNas and control mixtures that correspond to the titration curves in **c**. **e**, r_2 changes observed in HEPES buffer over multiple cycles of calcium (grey) or EDTA (white) addition, calibrated to alternate between 1 and 0 mM free Ca^{2+}.

(AFM) images further confirmed the nanoparticle aggregation in the presence of Ca^{2+} (Fig. 1b).

MaCaReNa responses were readily detectable by MRI, with a calcium-dependent increase in the strength of the contrast agent (transverse relaxivity, r_2) from $151 \pm 15\ mM^{-1}s^{-1}$ at 0 mM Ca^{2+} to $261 \pm 21\ mM^{-1}s^{-1}$ at 1.2 mM Ca^{2+} (Fig. 1c). This increase in r_2 is consistent with the expected consequences of aggregation for magnetic nanoparticles with diameter below ~30 nm (ref. [18]). Half-maximal r_2 changes were observed at 0.43 mM Ca^{2+}. Calcium-dependent r_2 changes could not be observed in samples that contained LCIOs without C2AB, or LCIOs mixed with a C2AB variant ($C2AB^{Ca-}$) engineered to lack calcium-binding affinity (Supplementary Fig. 2 and Supplementary Table 1). These controls demonstrate the specificity of calcium detection by the MaCaReNa mechanism. Raw images of samples that contain MaCaReNas or control mixtures show the corresponding T_2-weighted MRI signal changes in each case (Fig. 1d). Importantly, calcium-dependent r_2 changes could be reversed by the subsequent addition of excess ethylenediaminetetraacetic acid (EDTA), and restored again by further addition of excess $CaCl_2$ (Fig. 1e).

Response kinetics of the MaCaReNa probes are important for dynamic calcium sensing. To measure sensor-response times, we performed DLS experiments in which calcium concentrations were rapidly increased or decreased by the addition of Ca^{2+} or a chelator, respectively, to MaCaReNa samples that again contained 1 nM LCIOs and 2.5 μM C2AB (Supplementary Fig. 3a). The results indicated substantial changes in the light scattering that reflected clustering and unclustering of the sensors within the experimental dead time of ~20 s. Kinetic measurements of the LCIO–C2AB interaction on a faster timescale were obtained by measuring biolayer interferometry (BLI) changes after the rapid immersion of a surface conjugated to C2AB into a solution that contained LCIO particles (Supplementary Fig. 3b). The observed time intervals for half-maximal binding or dissociation of the particles were 4.9 ± 1.0 s and 4.1 ± 0.4 s, respectively. These results indicate that MaCaReNas formed from C2AB and LCIOs can achieve response rates suitable for calcium-dependent molecular-level functional MRI (molecular fMRI) on the timescale of seconds[2].

To ascertain whether aggregated versus disaggregated probe states could be distinguished by MRI in living tissue, we intracranially injected rats over one hour with a total of 7.2 μl of 1 nM LCIOs in the presence or absence of 2.5 μM C2AB. To prevent the agglomeration of particles before or during brain infusion, sensors and control samples were formulated in calcium-free aCSF that contained 5 mM ethylene glycol-bis(2-aminoethylether)-*N*,*N*,*N*′,*N*′-tetraacetic acid (EGTA). Volumetric analysis of the T_2-weighted MRI scans showed detectable contrast effects over regions of $80 \pm 60\ \mu l^3$ (Supplementary Fig. 4), which demonstrates the distribution of MaCaReNas over sizable measurement volumes in vivo is feasible. The region of contrast created by nanoparticle injection arose from convective spreading under the injection conditions we employed; because of parenchymal geometric constraints[19] and the relatively slow predicted diffusion of both MaCaReNa components[20], passive transport is unlikely to contribute significantly to the probe distribution or to the separation of LCIO and C2AB species from one another. The T_2-weighted MRI signal in areas infused

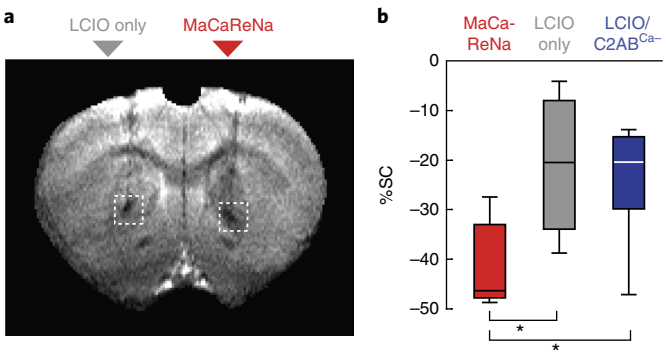

Fig. 2 | MaCaReNa calcium-binding activity correlates with MRI contrast in vivo. a, Injection of MaCaReNas into a rat brain (right) induces a substantially greater signal decrease than the injection of LCIO nanoparticles alone (left). **b**, Mean signal changes (%SC) after the intracranial injection of MaCaReNas ($n = 7$), LCIOs alone ($n = 4$) or calcium-insensitive $LCIO/C2AB^{Ca-}$ mixtures ($n = 5$) were quantified in ROIs comparable to the dotted white boxes in **a**. Box plots indicate the median (centre line), first and third quartiles (box edges) and full data ranges (whiskers). The differences between the MaCaReNas and both control conditions were significant ($P \leq 0.023$).

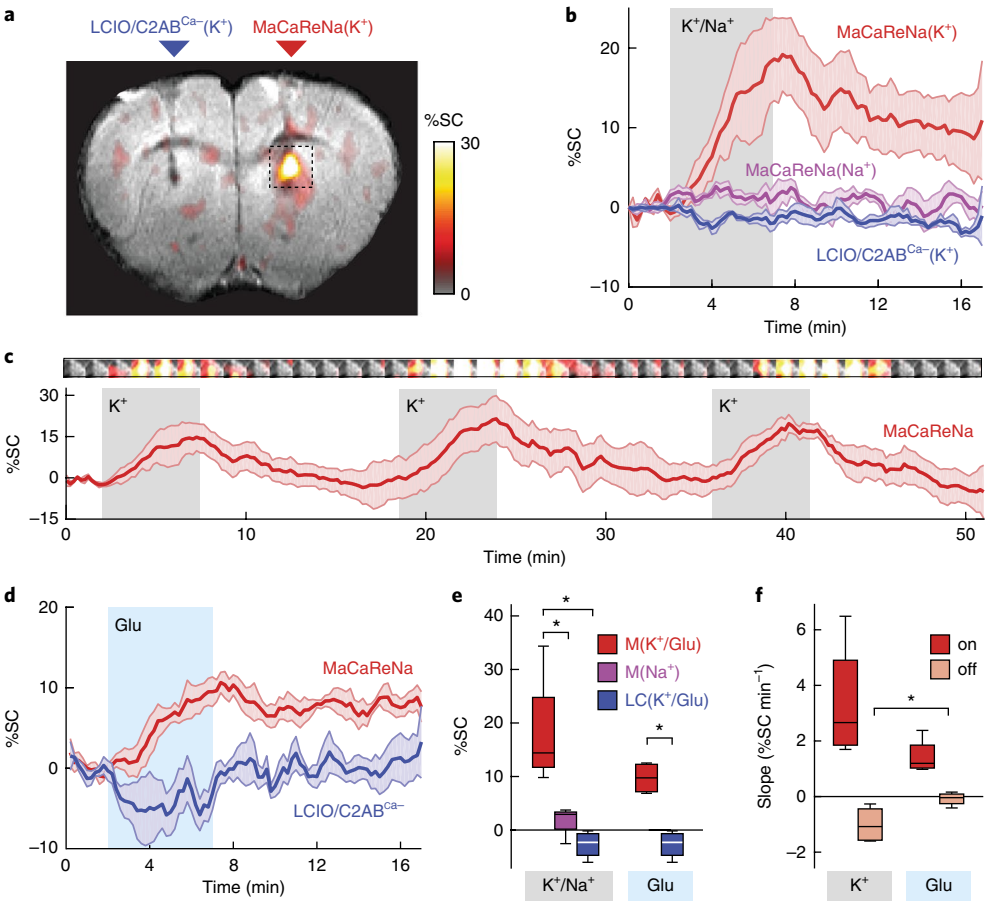

Fig. 3 | MaCaReNas report dynamic Ca^{2+} fluctuations in living rat brains. a, K^+ infusion (100 mM, 0.12 µl min^{-1}) induces molecular fMRI signal increases in the presence of MaCaReNa sensors (right) but not calcium-insensitive LCIO/C2AB^{Ca-} controls (left). Signal-change (%SC) amplitudes indicated by the colour scale are superimposed on a greyscale anatomical image for a representative rat (out of four). **b**, Signal-change time courses near areas of contrast-agent delivery show that K^+ infusion (grey shading) in the presence of MaCaReNas induces clear responses (red trace), whereas 100 mM Na^+ infusion in the presence of MaCaReNas (purple trace) and K^+ infusion in the presence of LCIO/C2AB^{Ca-} (blue trace) controls barely affect the MRI signal. **c**, The average time course of three consecutive K^+ stimuli (grey shading) shows the reproducibility of MaCaReNa responses ($n = 4$). The images above the trace correspond to the dotted box in **a** and illustrate the mean signal change from the pre-stimulus baseline as a function of time (average of 1.4 min per image frame). **d**, Dynamic signal changes in response to brain stimulation by glutamate infusion (1 mM, 0.12 µl min^{-1}) in the presence of MaCaReNas (red trace) and in the presence of LCIO/C2AB^{Ca-} (blue trace). **e**, Average signal changes (response at the stimulus offset time minus the baseline) measured under each of the stimulation conditions in **b** and **d**. MaCaReNas (M) in the presence of K^+ or glutamate (Glu) were significantly different from the LCIO/C2AB^{Ca-} controls (LC) and MaCaReNas in the presence of Na^+ ($P \leq 0.027$, $n = 4$ for all groups). **f**, Comparison of the slopes for the response onset (dark red) and recovery (light red) for K^+ and glutamate stimulation. The recovery slopes were significantly less negative for glutamate stimulation, indicative of a longer lasting $[Ca^{2+}]_o$ depression ($P = 0.04$, $n = 4$). All the shading indicates the s.e.m.; box plots indicate the median (centre line), first and third quartiles (box edges) and full data ranges (whiskers).

with MaCaReNas was considerably lower than in areas infused with LCIO only (Fig. 2a). A mean MRI signal decrease with respect to the background of 42 ± 4% was observed in brain areas infused with MaCaReNas; this change was significantly greater (*t*-test, $P \leq 0.023$, $n \geq 4$) than signal changes observed in areas injected with LCIOs only (21 ± 8%) or with LCIOs mixed with C2AB^{Ca-} (24 ± 6%) (Fig. 2b). These results suggest functionality of the MaCaReNa calcium-responsive mechanism in the living tissue.

To assess the ability of MaCaReNas to report dynamic changes in $[Ca^{2+}]_o$ evoked by neural activity, probes were injected intracranially into the rat striatum, followed by chemical neurostimulation using 0.6 µl pulses of 100 mM KCl in aCSF. A similar K^+ infusion paradigm has been used previously to induce neural-activity changes with a radius of over 1.5 mm (ref. [21]). In our experiments, K^+ stimulation produced notable signal increases exclusively within areas infused with MaCaReNas (Fig. 3a), consistent with the expected suppression of $[Ca^{2+}]_o$ by the stimulation and consequent decrease in r_2 due to disaggregation of the calcium sensors. Stimulus-dependent signal changes were reversible and could be repeated over multiple cycles of K^+ stimulation and recovery with no apparent decrease in response amplitudes over the repeated treatments (Fig. 3b,c). The observed rise times and decay times on the order of minutes probably reflect a mixture of K^+ infusion dynamics, neural-activity time courses and sensor-response characteristics. Corresponding K^+-induced MRI changes could not be observed in the presence of control sensors formulated with C2AB^{Ca-} (Fig. 3a,b). Similarly, signal changes were not observed after mock stimulation by the infusion of aCSF supplemented by 100 mM NaCl in place of KCl (Fig. 3b). Brain stimulation with 0.6 µl pulses of the excitatory neurotransmitter glutamate[22] (1 mM) also produced clear and repeatable signal increases in the presence of MaCaReNa sensors that could not be observed with the C2AB^{Ca-} control probes (Fig. 3d and Supplementary Fig. 5). Neither K^+ nor glutamate-dependent responses could be explained by direct effects of these stimulants

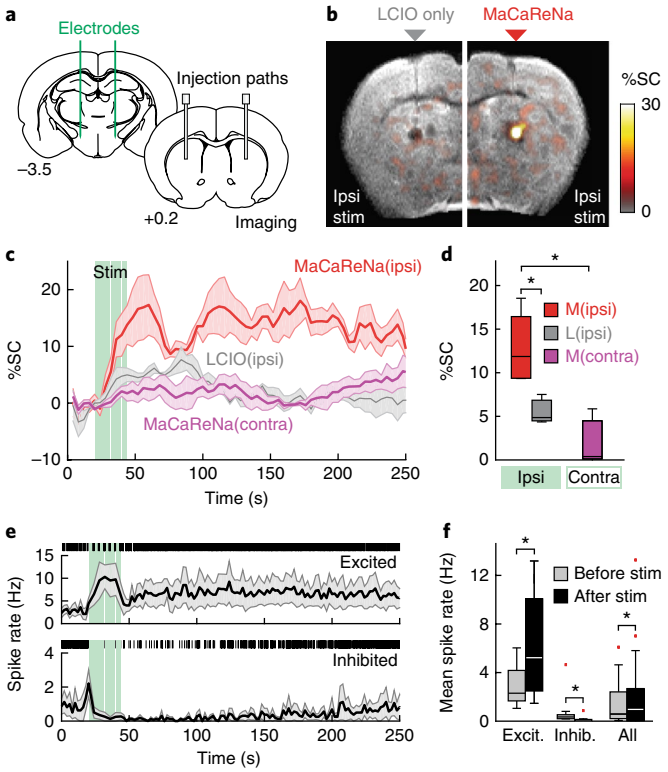

Fig. 4 | MaCaReNas report striatal responses to medial forebrain stimulation. a, The schematic shows locations of bilateral MFB electrode implantation and striatal MaCaReNa infusion; the distance from bregma is given below each brain section. **b**, Ipsilateral (ipsi) MFB stimulation (stim) induces MRI signal changes in the presence of MaCaReNas (right) but not of control LCIO particles (left). The mean signal changes (%SC) from four animals are shown in colour, superimposed over a T_2-weighted scan. **c**, Average response to ipsilateral (red) or contralateral (contra, purple) MFB stimulation in the presence of MaCaReNas, and response to ipsilateral stimulation in the presence of control LCIO particles (grey). Stimulus pulse trains are indicated by green vertical lines; shaded regions indicate the s.e.m. over multiple animals ($n=4$ for MaCaReNas, $n=3$ for controls). **d**, Mean signal changes during the immediate post-stimulus interval for all the conditions. MaCaReNas with ipsilateral stimulation were significantly different from both the contralateral stimulation condition and the LCIO control result ($P<0.05$). **e**, Single-unit recordings in the dorsal striatum using the MFB-stimulus paradigm. Prolonged post-stimulus excitation (top) or depression (bottom) of the subpopulations of units parallels the molecular fMRI time course. Mean spike rates are shown with the s.e.m. over the units (shading); representative rasters are shown above each time course. **f**, Mean spike rates before versus after the MFB stimulation for the excited units ($n=9$), inhibited units ($n=12$) and all the units ($n=38$) recorded from two animals. All the differences were significant with $P<0.0001$ when comparing 30 two-second bins before versus after stimulation. Box plots indicate the median (centre line), first and third quartiles (box edges) and full data ranges (whiskers), excluding outliers denoted by red squares.

on the MaCaReNas themselves (Supplementary Fig. 6). These measurements, therefore, indicate the ability of MaCaReNas to report neural-activity-dependent $[Ca^{2+}]_o$ fluctuations in the absence of artefacts from endogenous blood flow or other confounding factors.

Molecular fMRI signal changes induced by K^+ stimulation in the presence of MaCaReNas ($18\pm5\%$) were significantly greater than the signal changes induced by Na^+ infusion in the presence of MaCaReNas (t-test, $P=0.027$, $n=4$) or K^+ stimulation in the presence of control sensors formulated with $C2AB^{Ca-}$ (t-test, $P=0.0099$, $n=4$) (Fig. 3e). Glutamate-induced signal changes ($10\pm1\%$) were also significantly greater in the presence of MaCaReNas than in the presence of LCIO/$C2AB^{Ca-}$ mixtures (t-test, $P=0.0008$, $n=4$) (Fig. 3e). The varying effects of K^+ and glutamate stimulation were also reflected by differences in the slopes of the onset of signal changes observed during and after stimulation (Fig. 3f). Potassium stimulation evoked a sharper rise in the MRI signal, consistent with the greater magnitude of its effect, but its decline to baseline was also faster as a percentage of its rise time ($-30\pm4\%$ min^{-1} for K^+ versus $-2\pm4\%$ min^{-1} for glutamate), consistent with the possibility that glutamate-induced $[Ca^{2+}]_o$ depression might persist for longer in the brain.

To probe the ability of MaCaReNas to detect more physiological neuronal activation on a faster timescale, we applied the probes in conjunction with medial forebrain bundle (MFB) electrical stimulation[23], a neural activation paradigm used commonly in addiction research (Fig. 4a). Stimulation parameters chosen for the experiments were within the range of previous studies[24,25], and suitable for evoking robust self-stimulation behaviour in a standard operant paradigm (Supplementary Fig. 7), which demonstrates their relevance to naturalistic behaviour and its underlying neurophysiology. To measure calcium responses to the stimulation, MaCaReNas were infused into the dorsal striatum and then imaged using a block-design paradigm[26] in conjunction with T_2-weighted spin-echo echo-planar imaging performed with a frame rate of 0.25 Hz, which is also characteristic of conventional haemodynamic fMRI. Image-contrast changes were observed only when functional MaCaReNas were infused ipsilaterally to the stimulated MFB, and not under control conditions with the contralateral stimulation or calcium-insensitive LCIOs (Fig. 4b–d). The magnitude of the average observed response was $13\pm2\%$, comparable to the chemical stimulation paradigms of Fig. 3, but here the response was evoked within seconds and peaked near the stimulus offset time (Fig. 4c). This onset profile is similar to that reported previously using a closely related stimulation paradigm in conjunction with a dopamine-sensitive MRI contrast agent[24], which reflects the possibility that activation of the MFB dopamine fibres contributes substantially to the observed calcium response.

Unlike dopamine time courses, which return to the baseline shortly after MFB stimulation, the calcium-dependent signal remained elevated above the baseline for several minutes before decreasing again, which suggests that $[Ca^{2+}]_o$ stays suppressed over this time. To determine whether this prolonged effect is truly indicative of the underlying cellular activity, we recorded single-unit activity from the dorsal striatum during the same stimulus paradigm as used for the molecular fMRI experiments. Measurements revealed that many striatal neurons experienced firing-rate changes that persisted for about 2–3 min after the MFB stimulus, which parallels the MRI results (Fig. 4e). Though subsets of the neuronal population showed increases or decreases in activity, the overall population showed a 26% increase in the mean firing rate, which was highly significant with t-test $P<0.0001$ (Fig. 4f). Comparisons between pre- and post-stimulus average spike rates were highly significant in all three groups, with t-test $P<0.0001$. The trends in neural spike rates we observed were qualitatively comparable to previously published recordings that demonstrated protracted changes in neuronal firing in multiple brain regions after MFB stimulation[27,28]. These results thus suggest that the time course of MaCaReNa responses primarily reflects the natural dynamics of neural activity elicited by MFB stimulation, and perhaps arise in part from postsynaptic striatal dopamine-receptor activation, rather than from the kinetic characteristics of the sensors themselves.

Our findings thus demonstrate a molecular-imaging paradigm suitable for monitoring $[Ca^{2+}]_o$ dynamics in the interstitial space of the brain over biologically relevant intervals that range from seconds to hours[4,10]. In doing so, the work extends an emerging set of methods available for molecular fMRI[2]. In addition, the results establish that

MRI sensors based on magnetic nanoparticle aggregation can function reversibly in complex biological tissue, a principle that can apply to mechanistically related probes[29]. Though the biological side effects of MaCaReNas were not ruled out explicitly, the probe doses used here were too low to perturb substantially the $[Ca^{2+}]_o$ homeostasis through buffering (the Ca^{2+}-binding capacity of the injected sensors was <10 μM), and previous studies found that coated nanoparticles in the applied concentration range exhibit little toxicity[30].

Future applications of MaCaReNa imaging could include the characterization of extracellular calcium signalling in animal models, mechanisms that govern $[Ca^{2+}]_o$ fluctuations and relationships of extracellular calcium to diverse biological phenomena in the brain and other organs. Future work should also address current challenges of the method, such as a need for faster measurements and a more-rigorous quantification of $[Ca^{2+}]_o$. Building on the initial results presented here, MaCaReNas could be optimized further for neuroimaging applications by tuning their Ca^{2+} affinities more precisely to concentrations in the 0.8–1.2 mM range and by reducing the particle size to promote faster response kinetics and an improved probe distribution. Minimally invasive or fully non-invasive probe-delivery methods, such as those that employ ultrasound-assisted or receptor-mediated trans-blood–brain barrier transport, will also be important for applications that take full advantage of the whole-brain imaging capabilities of MRI.

Methods

Methods, including statements of data availability and any associated accession codes and references, are available at https://doi.org/10.1038/s41565-018-0092-4.

Received: 4 October 2016; Accepted: 13 February 2018;
Published online: 30 April 2018

References

1. Südhof, T. C. Calcium control of neurotransmitter release. *Cold Spring Harb. Perspect. Biol.* **4**, a011353 (2012).
2. Bartelle, B. B., Barandov, A. & Jasanoff, A. Molecular fMRI. *J. Neurosci.* **36**, 4139–4148 (2016).
3. Rusakov, D. A. Depletion of extracellular Ca^{2+} prompts astroglia to moderate synaptic network activity. *Sci. Signal* **5**, pe4 (2012).
4. Nicholson, C., Bruggencate, G. T., Steinberg, R. & Stöckle, H. Calcium modulation in brain extracellular microenvironment demonstrated with ion-selective micropipette. *Proc. Natl Acad. Sci. USA* **74**, 1287–1290 (1977).
5. Smith, S. M. et al. Calcium regulation of spontaneous and asynchronous neurotransmitter release. *Cell Calcium* **52**, 226–233 (2012).
6. Jones, B. L. & Smith, S. M. Calcium-sensing receptor: a key target for extracellular calcium signaling in neurons. *Front. Physiol.* **7**, 116 (2016).
7. Urwyler, S. Allosteric modulation of family C G-protein-coupled receptors: from molecular insights to therapeutic perspectives. *Pharmacol. Rev.* **63**, 59–126 (2011).
8. Egelman, D. M. & Montague, P. R. Calcium dynamics in the extracellular space of mammalian neural tissue. *Biophys. J.* **76**, 1856–1867 (1999).
9. Wiest, M. C., Eagleman, D. M., King, R. D. & Montague, P. R. Dendritic spikes and their influence on extracellular calcium signaling. *J. Neurophysiol.* **83**, 1329–1337 (2000).
10. Ding, F. et al. Changes in the composition of brain interstitial ions control the sleep–wake cycle. *Science* **352**, 550–555 (2016).
11. Dal Prà, I. et al. Calcium-sensing receptors of human astrocyte–neuron teams: amyloid-β-driven mediators and therapeutic targets of Alzheimer's disease. *Curr. Neuropharmacol.* **12**, 353–364 (2014).
12. Li, W.-H., Fraser, S. E. & Meade, T. J. A calcium-sensitive magnetic resonance imaging contrast agent. *J. Am. Chem. Soc.* **121**, 1413–1414 (1999).
13. Atanasijevic, T., Shusteff, M., Fam, P. & Jasanoff, A. Calcium-sensitive MRI contrast agents based on superparamagnetic iron oxide nanoparticles and calmodulin. *Proc. Natl Acad. Sci. USA* **103**, 14707–14712 (2006).
14. Mamedov, I. et al. In vivo characterization of a smart MRI agent that displays an inverse response to calcium concentration. *ACS Chem. Neurosci.* **1**, 819–828 (2010).
15. Johnson, I. & Spence, M. T. Z. *The Molecular Probes Handbook: A Guide to Fluorescent Probes and Labeling Technologies* 11th edn (Life Technologies, Waltham, 2010).
16. Diao, J., Yoon, T.-Y., Su, Z., Shin, Y.-K. & Ha, T. C2AB: a molecular glue for lipid vesicles with a negatively charged surface. *Langmuir* **25**, 7177–80 (2009).
17. Lee, J., Guan, Z., Akbergenova, Y. & Littleton, J. T. Genetic analysis of synaptotagmin C2 domain specificity in regulating spontaneous and evoked neurotransmitter release. *J. Neurosci.* **33**, 187–200 (2013).
18. Matsumoto, Y. & Jasanoff, A. T_2 relaxation induced by clusters of superparamagnetic nanoparticles: Monte Carlo simulations. *Magn. Reson. Imaging* **26**, 994–998 (2008).
19. Syková, E. & Nicholson, C. Diffusion in brain extracellular space. *Physiol. Rev.* **88**, 1277–1340 (2008).
20. Tyn, M. T. & Gusek, T. W. Prediction of diffusion coefficients of proteins. *Biotechnol. Bioeng.* **35**, 327–338 (1990).
21. Adámek, S. & Vyskočil, F. Potassium-selective microelectrode revealed difference in threshold potassium concentration for cortical spreading depression in female and male rat brain. *Brain Res.* **1370**, 215–219 (2011).
22. Ciriello, J. & Janssen, S. A. Effect of glutamate stimulation of bed nucleus of the stria terminalis on arterial pressure and heart rate. *Am. J. Physiol.* **265**, H1516–H1522 (1993).
23. Olds, J. & Milner, P. Positive reinforcement produced by electrical stimulation of septal area and other regions of rat brain. *J. Comp. Physiol. Psychol.* **47**, 419–427 (1954).
24. Lee, T., Cai, L. X., Lelyveld, V. S., Hai, A. & Jasanoff, A. Molecular-level functional magnetic resonance imaging of dopaminergic signaling. *Science* **344**, 533–535 (2014).
25. Fiallos, A. M. et al. Reward magnitude tracking by neural populations in ventral striatum. *NeuroImage* **146**, 1003–1015 (2017).
26. Penny, W. D., Friston, K. J., Ashburner, J. T., Kiebel, S. & Nichols, T. E. *Statistical Parametric Mapping: The Analysis of Functional Brain Images* (Academic Press, Cambridge, 2011).
27. Keene, J. J. Prolonged unit responses in thalamic reticular, ventral, and posterior nuclei following lateral hypothalamic and midbrain reticular stimulation. *J. Neurosci. Res.* **1**, 459–469 (1975).
28. Keene, J. J. Prolonged medial forebrain bundle unit responses to rewarding and aversive intracranial stimuli. *Brain Res. Bull.* **1**, 517–522 (1976).
29. Haun, J. B., Yoon, T.-J., Lee, H. & Weissleder, R. Magnetic nanoparticle biosensors. *Wiley Interdiscip. Rev. Nanomed. Nanobiotechnol.* **2**, 291–304 (2010).
30. Lewinski, N., Colvin, V. & Drezek, R. Cytotoxicity of nanoparticles. *Small* **4**, 26–49 (2008).

Acknowledgements

Project funding was provided by NIH grants R01-DA038642, DP2-OD2114, BRAIN Initiative award U01-NS090451 and an MIT Simons Center for the Social Brain Seed Grant to A.J., as well as NIH grant R01-EY007023 to M.S. S.O. was supported by RGO, a JSPS Postdoctoral Fellowship for Research Abroad and an Uehara Memorial Foundation postdoctoral fellowship. E.R. was supported by a Beatriu de Pinós Fellowship from the Government of Catalonia. We thank W. White for assistance with the BLI experiments, S. Bricault for help with data analysis and D. Pheasant at the MIT Biophysical Instrumentation Facility (BIF) for training and assistance with circular dichroism and BLI measurements; BIF instruments are available thanks to NSF grant 0070319 and NIH grant S10-OD016326. We are grateful to J. T. Littleton and J. Lee for supplying the C2AB-expression clone.

Author contributions

S.O., J.J.L., B.B.B. and E.R. performed the in vitro experiments. B.B.B. and J.M. performed the ex vivo experiments. B.B.B., N.L. and S.O. performed in vivo MRI. B.B.B., N.L. and V.B.-P. performed the electrophysiology with supervision and advice from M.S. S.O., B.B.B. and A.J. designed the research and wrote the paper.

Competing interests

The authors declare no competing interests.

Additional information

Supplementary information is available for this paper at https://doi.org/10.1038/s41565-018-0092-4.

Reprints and permissions information is available at www.nature.com/reprints.

Correspondence and requests for materials should be addressed to A.J.

Publisher's note: Springer Nature remains neutral with regard to jurisdictional claims in published maps and institutional affiliations.

Methods

Animals. All animal experiments were performed after the approval of the Massachusetts Institute of Technology (MIT) Committee on Animal Care, and in accordance with the institutional and National Institutes of Health (NIH) guidelines. A total of 26 rats were used for the data presented in this paper. All the animals were male Sprague-Dawley rats, 8–10 weeks of age; they were purchased from Charles River Laboratories. The animals were housed and maintained on a 12 h light/dark cycle with *ad libitum* access to food and water. Sample sizes for all the animal experiments were chosen such that between-group comparisons provided a power of 0.8 when detecting 10% signal differences between the groups using two-tailed *t*-tests with $\alpha = 0.05$, assuming within-group standard deviations of approximately 5%.

AFM. The sample solution (30 µl) was deposited onto a V-1 quality muscovite mica disc (Electron Microscopy Sciences) freshly cleaved using adhesive tape. The mica was incubated in a Petri dish for 30 min, rinsed with 1 ml of deionized water and then dried initially with compressed air. The mica was further dried overnight at room temperature and protected from dust contamination. The prepared sample was measured in air using a Multimode 8 atomic force microscope equipped with a SCANASYST-AIR cantilever (Bruker Instruments) operated in the soft tapping mode.

DLS. DLS was performed using a DynaPro DLS system (Wyatt Technology) with a 1 s integration time at 22 °C. The laser power was adjusted so that all the samples gave a scattering light intensity on the order of 10^5 counts s^{-1}.

Preparation of LCIOs. L-α-phosphatidylcholine (4.5 mg) from hen egg (Avanti Polar Lipids) and 1.5 mg of L-α-phosphatidylserine from porcine brain (Avanti Polar Lipids) were dissolved in 250 µl of chloroform. An aliquot (50 µl) of an iron oxide nanoparticle (10 nm with an oleic acid coating in chloroform, from Ocean NanoTech) solution (5 mg Fe ml^{-1}) was mixed with the lipid solution and the mixture was thoroughly evaporated to obtain an even brown lipid film. HEPES buffer (200 µl, 10 mM, pH 7.4) was added into the lipid film and sonicated until the entire brown layer was homogeneously dispersed into the buffer to yield a brown transparent solution. The mixture was inserted into a magnetic µ column, placed into a µMACS magnetic separator (Miltenyi Biotec) and washed four times with buffer aliquots (50 µl). The purified solution was eluted by removing the column from the magnet and adding 150 µl of the buffer. The eluate was centrifuged at 6,000*g* for 10 min to remove large aggregates and then the supernatant was filtered using a 0.1 µm syringe top filter. The final resulting concentration of LCIOs was quantified from the absorbance at 450 nm using a molar absorbance coefficient of $\varepsilon_{450} = 690\ (M\ Fe)^{-1}\ cm^{-1}$, which in turn was determined by a colorimetric assay using bathophenanthrolinedisulfonic acid[31].

Purification of C2AB. *Escherichia coli* (BL21) that express 6xHis-tagged C2AB were generously provided by J. Lee and J. T. Littleton (MIT). 6xHis-tagged C2AB was purified according to published procedures[17], with minor modifications. Briefly, *E. coli* cells that harboured the tagged C2AB gene were grown in 5 ml of lysogeny broth (LB) medium with 50 µg ml^{-1} of ampicillin at 37 °C overnight. LB/ampicillin medium (100 ml) was inoculated with 1 ml of the overnight culture and grown to $OD_{600} = 0.6$ for 2–3 h at 37 °C. Protein expression was induced by adding 1 ml of 1 M isopropyl-β-D-1-thiogalactopyranoside (IPTG) during vigorous shaking. The cells were harvested 4 h after adding IPTG by centrifugation at 6,000*g* for 20 min at 4 °C. The obtained cell pellet (~1 g) was stored at −80 °C overnight and subsequently lysed by the addition of 5 ml of BugBuster reagent (EMD Millipore), 10 µl of Lysonase Bioprocessing Reagent (EMD Millipore) and 50 µl of P8849 protease inhibitor cocktail (Sigma-Aldrich). The cell lysate was vortexed quickly and nutated gently for 15 min at room temperature. The mixture was then centrifuged at 12,000*g* for 20 min at 4 °C to pellet the insoluble material. The collected supernatant was added to a column partially filled with 1 ml of Ni-NTA Superflow Resin (Qiagen) previously pre-equilibrated with binding buffer (50 mM NaH_2PO_4, 300 mM NaCl, 10 mM imidazole, pH 8.0). The loaded column was nutated for 1 h at 4 °C to promote protein binding. The resin was washed four times using 5 ml of wash buffer (50 mM NaH_2PO_4, 300 mM NaCl, 20 mM imidazole, 0.1% Tween 20, pH 8.0) and four times using 5 ml of the wash buffer without Tween 20. Then, the protein was eluted by the addition of 1 ml of elution buffer (50 mM NaH_2PO_4, 300 mM NaCl, 250 mM imidazole, pH 8.0). The eluate was concentrated and exchanged into experimental buffer conditions using a 10 K Amicon Ultra filter (EMD Millipore). The protein purity was assessed by SDS–PAGE, and protein concentration was determined using the Pierce 660 nm Protein Assay (Thermo Fisher Scientific).

Cloning of $C2AB^{Ca-}$. The calcium-binding sites of C2AB were determined from structural data[32] and Ca^{2+}-binding residues were mutated to alanine in silico using Serial Cloner software (www.serialbasics.free.fr). The resulting mutant sequence was ordered as a synthetic DNA fragment (Integrated DNA Technologies). The fragment was ligated into the original C2AB plasmid using NEBuilder assembly enzymes (New England Biolabs).

BLI. BLI was performed on an Octet Red BLI instrument (Pall ForteBio). C2AB was attached to the sensor probes via adhesion to an Ni-NTA-coated tip. Binding kinetics were monitored after submersion of the C2AB-bound tip in aCSF that contained 1.2 mM Ca^{2+} and 1 nM LCIOs (100 µM Fe). The dissociation rates were measured by then transferring the tips to calcium-free aCSF after briefly washing excess LCIOs off in complete aCSF. Kinetics data were analysed using custom-written MATLAB (MathWorks) scripts.

In vitro MRI. In vitro MRI was performed with a 7 T Biospec MRI scanner (Bruker). Samples were arrayed into bisected 384-well microtiter plates and imaged using a volume tranceiver coil. A multislice multiecho pulse sequence was used to obtain T_2-weighted images, with typical parameters including matrix size = 256 × 256, field of view (FOV) = 5 cm × 5 cm, slice thickness = 2 mm, repetition time (*TR*) = 2,000 ms, echo spacing with echo time (*TE*) = 8 ms, and number of echoes = 30. T_2 values were obtained by exponential fitting to MRI intensities as a function of *TE*. r_2 values were defined by two-point measurements of the slopes between $1/T_2$ of aCSF without nanoparticles and $1/T_2$ of aCSF that contained 100 µM Fe nanoparticles, and are reported as the mean and s.e.m. of measurements performed in triplicate. r_2 titrations were performed in aCSF with varying concentrations of calcium. Measurement of the reversibility of r_2 changes was performed in 10 mM HEPES, 150 mM NaCl, pH 7.4, with the addition of excesses of $CaCl_2$ and EDTA to achieve an alternation between 0 mM and 1 mM net Ca^{2+} concentrations. The use of a lower ionic strength buffer for this experiment limited the effects of the accumulation of $CaCl_2$ and EDTA throughout the procedure, but resulted in slightly greater r_2 values than observed in aCSF under high calcium conditions.

Ex vivo MRI and analysis of nanoparticle infusion. To measure brain volumes affected by the infusion of nanoparticle mixtures, animals were injected with 200/10 mg/kg ketamine/xylazine after MRI experiments and cardiac perfused with cold phosphate-buffered saline with 10 units ml^{-1} heparin followed by 4% paraformaldehyde. The animals were then prepared for high-resolution post-mortem imaging according to published procedures[33]. The animals were decapitated and tissue was stripped from the skull before incubating in 1 mM gadolinium diethylenetriaminepentaacetic acid for 96 h at 4 °C. The resulting fixed, contrast-enhanced samples were then scanned with 100 µm isotropic resolution using a gradient echo-pulse sequence implemented with *TR*/*TE* = 250/35 ms on the 7 T scanner. Rat brains were manually segmented for analysis and areas of hypointensity were further segmented from the three-dimensional (3D) data sets by placing a seed value at the centre of the injection area with a threshold at ±10% of the seed signal intensity. All the 3D analysis was done using the segmentation editor in FIJI (http://fiji.sc/).

Cannula implantation and brain infusion of nanoparticle mixtures. The nanoparticle mixtures formulated for brain infusion included 1 nM LCIOs (100 µM Fe) alone or mixed with 2.5 µM C2AB protein (for MaCaReNas) or 2.5 µM $C2AB^{Ca-}$ (for the control LCIO/$C2AB^{Ca-}$ mixtures). All of these mixtures were formulated in calcium-free aCSF (125 mM NaCl, 2.5 mM KCl, 1 mM $MgCl_2$, 1.25 mM NaH_2PO_4, 25 mM $NaHCO_3$), supplemented with 5 mM EGTA. Prior to infusion of these solutions, animals were anaesthetized with ~2% isoflurane, shaved, and mounted in a rodent stereotaxic device (David Kopf Instruments); heart rates and blood oxygenation were monitored by a pulse oximeter (Nonin Medical). Each animal's scalp was retracted and 28 G holes were drilled into the skull above desired injection sites. 28 guage cannula guides (Plastics One) that projected 2 mm below the surface of the skull were implanted using SEcure light curing dental cement (Parkell) and 33 guage metal injection cannulae that projected 5 mm below the skull were lowered to the appropriate depth through the holes. All the injections were targeted to the caudate nucleus, coordinates 1 mm anterior, 3 mm lateral and 5 mm ventral to the bregma, chosen based on a standard rat-brain atlas[34]. Nanoparticle infusions were performed using an injection rate of 0.12 µl min^{-1} for 1 h with the control and test sides alternated for each experiment to negate potential artefacts or bias. Metal cannulae were then removed and the animals were transferred to an MRI rat-imaging cradle (Bruker). Plastic cannulae for the delivery of the control and stimulatory agents during MRI were then lowered bilaterally through the guide cannulae to the contrast-agent delivery sites, and subsequently fixed in place with ETC light-curing dental cement (Parkell).

Calcium-dependent molecular fMRI with chemical brain stimulation. In vivo MRI measurements were obtained using a 9.4 T Biospec MRI scanner (Bruker) operated with a cross-coil volume transmit, surface-receive configuration. Rapid acquisition with refocused echoes (RARE) pulse sequences were used to acquire T_2-weighted anatomical and functional images. Imaging parameters for anatomical images included a number of averages = 6, matrix size = 300 × 200, FOV = 3 cm × 2 cm, slice thickness = 1.2 mm, *TR* = 5,000 ms, effective *TE* = 60 ms, and RARE factor = 8. The imaging parameters for the functional imaging scan series were matrix size = 75 × 50, FOV = 3 cm × 2 cm, slice thickness = 1.2 mm, *TR* = 3,000 ms, effective *TE* = 90, and RARE factor = 8. The acquisition time per image frame was 12 s. Chemical stimuli delivered during molecular fMRI experiments consisted of pulsed injections of complete aCSF supplemented by 100 mM KCl, 100 mM NaCl (control) or 1 mM glutamate, and delivered at a rate of 0.12 µl min^{-1} during continuous image acquisition. Each experiment consisted of a

2 min pre-stimulation period, followed by 5 min of stimulation and 10 min of rest. Three stimulations were performed for each animal.

Calcium-dependent molecular fMRI with electrical brain stimulation. Rats were purchased with pre-implanted jugular catheters (Charles River Laboratories). After acclimation, unipolar electrodes were implanted bilaterally into the MFB. Guide cannulae for striatal sensor infusion were implanted as described above, and headposts to fix the heads in place during the imaging were attached above the sagittal suture using dental cement. The rats were allowed 3–7 d for recovery, and then anaesthetized and infused with MaCaReNa sensor doses as per previous methods. The animals were then intubated via a tracheotomy, transferred to lighter chemical anaesthesia with 1 mg kg^{-1} intraperitoneal (i.p.) medetomidine and paralysed with pancuronium (2 m kg^{-1} i.p.) to prevent motion artefacts during the stimulation. On paralysis, the animals were transferred to a small animal respirator (Harvard Apparatus Inspira) and fixed, via their headposts, into a custom-built cradle for imaging. Once positioned in the magnet, medetomidine (1 mg^{-1} kg h^{-1}) and pancuronium (2 mg kg^{-1} h^{-1}) were delivered continuously via an i.p. catheter, along with N^{ω}-nitro-L-arginine methyl ester (100 mg kg^{-1} h^{-1} intravenously) to suppress the haemodynamic signals. After 45 min of acclimation to these conditions, functional imaging was performed using T_2-weighted spin-echo echo-planar imaging (TE = 60 ms, TR = 4 s). During each animal's scan session, the stimulation was applied in five epochs that consisted of a 2 min baseline, 24 s MFB stimulation (0.3 mA, 200 Hz, 1 ms pulses, 75% duty cycle that consisted of 3 s trains separated by 1 s between trains) and then 5 min of recovery before the next epoch.

Electrophysiology with electrical brain stimulation. Animals were prepared similarly to those for the MRI studies. Immediately after implantation of the stimulation electrodes, the animals were paralysed, and their anaesthesia was switched to medetomidine. Using a micromanipulator Sutter Instrument Company MP-285, a 16-channel laminar probe (Neuronexus Technologies A1x16-10mm-100-177-A16) was lowered into the dorsal striatum (~5 mm) through a previously drilled craniotomy (0.2 mm anterior and 3.0 mm lateral to the bregma). Extracellular signals recorded via the electrodes were amplified using a 1 × gain headstage (Plexon model E2a) connected to a 50 × preamp (Plexon PBX-247) and digitized at 50 kHz. A 250 Hz high-pass filter was applied to the raw signal, and single units were sorted using the Offline Sorter software (Plexon) based on their principal components, peak valley and non-linear energy ratio prior to sorting units. Time stamps of the sorted units were exported to MATLAB and post-stimulus time histograms and further statistics were computed using custom procedures. The sample sizes of neurons were chosen such that between-group comparisons provided a power of 0.95 and significance was defined by two-tailed t-tests with $\alpha = 0.05$.

Behavioural assessment of intracranial self-stimulation. Behaviour experiments were performed in a 28 × 21 × 21 cm plexiglass operant chamber (Lafayette Instruments). One infrared nose-poke sensor was positioned at one end of the operant chamber. Input from the nose-poke sensor was recorded via a digital input/output interface (National Instruments). This input triggered MFB stimulation in 3 s trains of 200 Hz, 0.3 mA and 1 ms electrical pulses, identical to the stimuli used in the fMRI experiments. Two animals were shaped to the task and then tested over ten 60 s trials each, with an intertrial interval of 10 s. Input and output events for every trial were recorded and analysed by custom-written computer scripts implemented in C and MATLAB to generate the data presented in Supplementary Fig. 7.

MRI data analysis. Images were reconstructed using Paravision software (Bruker) and further analysed using custom routines implemented in MATLAB. For the quantitative analysis of signal changes induced by the injection of MaCaReNas, LCIOs or LCIO/C2AB^{Ca-} mixtures (Fig. 2), regions of interest (ROIs) were determined by manually selecting the centroids of the apparent nanoparticle-induced hypointensity from MRI images. Signal-change values were determined by averaging the observed intensities within a 3 × 3 pixel (1.2 × 1.2 mm) square around these centroids. In each case, the percent signal change (%SC) was determined as the difference between mean MRI intensity in each injection site ROI (S_{inj}) and the mean intensity in a reference ROI positioned medial to the infusion zones (S_{ref}), such that $\%SC = 100 \times (S_{inj} - S_{ref})/S_{ref}$. Reported values are averaged over animals, and given with corresponding s.e.m. values.

Quantitative analysis of the chemical stimulus-induced molecular fMRI signal changes (Fig. 3) was performed on data converted on a per-voxel basis to %SC from baseline, according to the relationship $\%SC = 100 \times [S(t) - S_{base}]/S_{base}$, where $S(t)$ is the signal at any arbitrary time point and S_{base} is the mean signal observed during the 2 min pre-stimulation period. Signal time courses for each animal were determined by manually selecting a brain hemisphere and then using an operator-blind algorithm to identify the centroids of apparent nanoparticle-induced hypointensity from the MRI images. This ROI was defined around the pixel of peak signal change averaged over 2 min, centred at the endpoint of injection and averaging the %SC values around this pixel over a 1.2 × 1.2 mm square ROI. These time courses were temporally smoothed over a moving window of 1 min, baseline corrected to remove linear drift (for multiple stimulus experiments only) and each series of stimulus responses was averaged over multiple animals to obtain the mean time courses and corresponding s.e.m. for each experimental condition. %SC amplitudes for each stimulus type were defined as $\%SC = 100 \times (S_{stim} - S_{base})/S_{base}$, where S_{base} is the MRI signal intensity observed during the 2 min pre-stimulus baseline and S_{stim} is the MRI signal observed during a 2 min window around the stimulant infusion offset time. Signal-change slopes associated with the response to and recovery from stimulation were determined by linear fitting to the 5 min stimulant infusion periods and 10 min post-infusion periods, respectively. The distributions of signal-change amplitudes and slope values from multiple animals are presented as box plots. Only experimental sessions that were prematurely terminated due to major technical failures were excluded from analysis.

For the MFB stimulation experiments of Fig. 4, baseline measurements, conversion to %SC and ROI selection were again performed as described above. Responses to all five stimuli presented to each animal were averaged together before the ROI analysis, and ROIs were centred around the pixel of maximum response within a 20 s window centred about the endpoint of the stimulation. Stimulation traces from each animal were averaged and smoothed over a 20 s window; the traces presented in Fig. 4c represent the mean and s.e.m. time courses from multiple animals. The %SC amplitudes presented in Fig. 4d were defined as $\%SC = 100 \times (S_{stim} - S_{base})/S_{base}$, where S_{base} is the mean baseline MRI signal intensity and S_{stim} is the MRI signal observed during a 60 s window beginning at the stimulus offset time; box plots depict data from multiple animals.

Life sciences reporting summary. Further information on experimental design is available in the Life Sciences Reporting Summary.

Code availability. Scripts used for data analysis are available on reasonable request.

Data availability. Expression-construct sequences and raw MRI datasets generated during and/or analysed during the current study are available from the corresponding author on reasonable request.

References

31. Tamarit, J., Irazusta, V., Moreno-Cermeño, A. & Ros, J. Colorimetric assay for the quantitation of iron in yeast. *Anal. Biochem.* **351**, 149–151 (2006).
32. Fuson, K. L., Montes, M., Robert, J. J. & Sutton, R. B. Structure of human synaptotagmin 1 C2AB in the absence of Ca^{2+} reveals a novel domain association. *Biochemistry* **46**, 13041–13048 (2007).
33. Szulc, K. U. et al. MRI analysis of cerebellar and vestibular developmental phenotypes in *Gbx2* conditional knockout mice. *Magn. Reson. Med.* **70**, 1707–1717 (2013).
34. Paxinos, G., & Watson, C. *The Rat Brain in Stereotaxic Coordinates: The New Coronal Set* 5th edn (Elsevier, Amsterdam, 2004).

nature research

Corresponding author(s): *Double-blind peer review submissions: write DBPR and your manuscript number here instead of author names.*

Life Sciences Reporting Summary

Nature Research wishes to improve the reproducibility of the work that we publish. This form is intended for publication with all accepted life science papers and provides structure for consistency and transparency in reporting. Every life science submission will use this form; some list items might not apply to an individual manuscript, but all fields must be completed for clarity.

For further information on the points included in this form, see Reporting Life Sciences Research. For further information on Nature Research policies, including our data availability policy, see Authors & Referees and the Editorial Policy Checklist.

Please do not complete any field with "not applicable" or n/a. Refer to the help text for what text to use if an item is not relevant to your study.

For final submission: please carefully check your responses for accuracy; you will not be able to make changes later.

Experimental design

1. Sample size

Describe how sample size was determined.

Sample sizes for all animal experiments were chosen such that between-group comparisons provided a power of 0.8 when detecting 10% signal differences between groups using two-tailed t-tests.

2. Data exclusions

Describe any data exclusions.

Only experimental sessions that were prematurely terminated due to major technical failures were excluded from analysis.

3. Replication

Describe the measures taken to verify the reproducibility of the experimental findings.

All experiments were performed with multiple replicates, and standard statistical methods were used to accept or reject null hypotheses of no effect.

4. Randomization

Describe how samples/organisms/participants were allocated into experimental groups.

n/a

5. Blinding

Describe whether the investigators were blinded to group allocation during data collection and/or analysis.

n/a

Note: all in vivo studies must report how sample size was determined and whether blinding and randomization were used.

6. Statistical parameters

For all figures and tables that use statistical methods, confirm that the following items are present in relevant figure legends (or in the Methods section if additional space is needed).

n/a	Confirmed
☐	☒ The exact sample size (*n*) for each experimental group/condition, given as a discrete number and unit of measurement (animals, litters, cultures, etc.)
☐	☒ A description of how samples were collected, noting whether measurements were taken from distinct samples or whether the same sample was measured repeatedly
☐	☒ A statement indicating how many times each experiment was replicated
☐	☒ The statistical test(s) used and whether they are one- or two-sided *Only common tests should be described solely by name; describe more complex techniques in the Methods section.*
☒	☐ A description of any assumptions or corrections, such as an adjustment for multiple comparisons
☐	☒ Test values indicating whether an effect is present *Provide confidence intervals or give results of significance tests (e.g. P values) as exact values whenever appropriate and with effect sizes noted.*
☐	☒ A clear description of statistics including central tendency (e.g. median, mean) and variation (e.g. standard deviation, interquartile range)
☐	☒ Clearly defined error bars in all relevant figure captions (with explicit mention of central tendency and variation)

See the web collection on statistics for biologists for further resources and guidance.

Software

Policy information about availability of computer code

7. Software

Describe the software used to analyze the data in this study.	MATLAB, custom scripts in C.

For manuscripts utilizing custom algorithms or software that are central to the paper but not yet described in the published literature, software must be made available to editors and reviewers upon request. We strongly encourage code deposition in a community repository (e.g. GitHub). *Nature Methods* guidance for providing algorithms and software for publication provides further information on this topic.

Materials and reagents

Policy information about availability of materials

8. Materials availability

Indicate whether there are restrictions on availability of unique materials or if these materials are only available for distribution by a third party.	Complete description of synthetic methods is provided. Additional materials are available upon reasonable request, according to standard material transfer procedures.

9. Antibodies

Describe the antibodies used and how they were validated for use in the system under study (i.e. assay and species).	n/a

10. Eukaryotic cell lines

a. State the source of each eukaryotic cell line used.	n/a
b. Describe the method of cell line authentication used.	n/a
c. Report whether the cell lines were tested for mycoplasma contamination.	n/a
d. If any of the cell lines used are listed in the database of commonly misidentified cell lines maintained by ICLAC, provide a scientific rationale for their use.	n/a

Animals and human research participants

Policy information about studies involving animals; when reporting animal research, follow the ARRIVE guidelines

11. Description of research animals

Provide all relevant details on animals and/or animal-derived materials used in the study.	All animals were male Sprague-Dawley rats, 8-10 weeks of age, purchased from Charles River Laboratories.

Policy information about studies involving human research participants

12. Description of human research participants

Describe the covariate-relevant population characteristics of the human research participants.	n/a